The Astrophysical Journal, 904:12 (8pp), 2020 November 20 https://doi.org/10.3847/1538-4357/abbc19

Kinetic Simulation of Nonrelativistic Perpendicular Shocks of Young Supernova Remnants. IV. Electron Heating

Artem Bohdan[1], Martin Pohl[1,2], Jacek Niemiec[3], Paul J. Morris[1], Yosuke Matsumoto[4], Takanobu Amano[5], and Masahiro Hoshino[5]
[1] DESY, D-15738 Zeuthen, Germany; artem.bohdan@desy.de
[2] Institute of Physics and Astronomy, University of Potsdam, D-14476 Potsdam, Germany
[3] Institute of Nuclear Physics Polish Academy of Sciences, PL-31342 Krakow, Poland
[4] Department of Physics, Chiba University, 1-33 Yayoi-cho, Inage-ku, Chiba 263-8522, Japan
[5] Department of Earth and Planetary Science, The University of Tokyo, 7-3-1 Hongo, Bunkyo-ku, Tokyo 113-0033, Japan
Received 2020 August 13; revised 2020 September 23; accepted 2020 September 24; published 2020 November 18

Abstract

High-Mach-number collisionless shocks are found in planetary systems and supernova remnants (SNRs). Electrons are heated at these shocks to temperatures well above the Rankine–Hugoniot prediction. However, the processes responsible for causing the electron heating are still not well understood. We use a set of large-scale particle-in-cell simulations of nonrelativistic shocks in the high-Mach-number regime to clarify the electron heating processes. The physical behavior of these shocks is defined by ion reflection at the shock ramp. Further interactions between the reflected ions and the upstream plasma excites electrostatic Buneman and two-stream ion–ion Weibel instabilities. Electrons are heated via shock surfing acceleration, the shock potential, magnetic reconnection, stochastic Fermi scattering, and shock compression. The main contributor is the shock potential. The magnetic field lines become tangled due to the Weibel instability, which allows for parallel electron heating by the shock potential. The constrained model of electron heating predicts an ion-to-electron temperature ratio within observed values at SNR shocks and in Saturn's bow shock.

Unified Astronomy Thesaurus concepts: Shocks (2086); Plasma astrophysics (1261); Supernova remnants (1667); Interstellar medium (847)

1. Introduction

Collisionless shocks are commonly observed in astrophysical environments such as planetary systems, supernova remnants (SNRs) and jets of active galactic nuclei when plasmas move with supersonic velocities. In such flows, collective particle interactions form a shock layer on kinetic plasma scales much smaller than the collisional mean free path. In the shock transition, part of the bulk kinetic energy is converted into energies of thermal particles and electromagnetic fields through wave–particle interactions. The microphysics of these processes is still not fully understood, especially in the high-Mach-number regime.

High-Mach-number shocks are supercritical, which means that the upstream kinetic energy cannot be entirely dissipated via Joule heating (ohmic dissipation). If the Mach number is above a certain limit ($M_s \gtrsim 2.76$; Marshall 1955) part of the kinetic energy is dissipated via ion reflection by the shock potential. In quasi-perpendicular shocks the interaction of reflected ions with the upstream plasma leads to the excitation of two-stream instabilities. The electrostatic Buneman instability (Buneman 1958) is excited at the leading edge of the shock foot and it results from interaction of the hot reflected ions and the cold upstream electrons. Deeper in the shock foot the interaction of reflected and upstream ions results in the ion–ion two-stream Weibel instability (Fried 1959). These instabilities shape the shock structure forming the shock foot with electrostatic Buneman waves and Weibel filamentary structures, strongly turbulent ramp and overshoot regions, and the shock downstream filled with thermalized plasma.

This paper is the fourth in a series of works focusing on the analysis of high-Mach-number perpendicular shock physics by dint of particle-in-cell (PIC) simulations. Previously (Bohdan et al. 2019a, 2019b, 2020, hereafter Papers I, II, and III) we discussed the processes responsible for producing nonthermal electrons, namely, shock surfing acceleration (SSA; Paper I) and its influence on the nonthermal downstream electron population (Paper II) and magnetic reconnection (Paper III). In these papers we have defined how the acceleration efficiencies depend on the sonic and Alfvénic Mach numbers and ion-to-electron mass ratio (hereafter referred to as the mass ratio). We found that regardless of the Mach number SSA negligibly contributes to the nonthermal electron population in perpendicular shocks given a realistic mass ratio. Magnetic reconnection appears to be very active and operates as an efficient electron accelerator in shocks with higher Mach numbers; however, the nonthermal electron production efficiency does not depend on the mass ratio used in simulations.

Here we study electron heating processes at high-Mach-number shocks with $M_A \gtrsim 20$. It was already reported that PIC simulations of low-Mach-number shocks (Tran & Sironi 2020) demonstrate good consistency of simulations and in situ measurements of Earth's (Schwartz et al. 1988) and Saturn's (Masters et al. 2011) bow shocks. The superadiabatic electron heating (above the limit predicted by the Rankine–Hugoniot condition) is associated with the cross-shock potential and interaction with ion-scale waves in the shock transition. However, there is a lack of understanding in how electrons are heated in the high-Mach-number regime.

If no energy exchange between electrons and ions is expected in the shock transition region, then the downstream electron temperature is described by the Rankine–Hugoniot condition. Observations of Balmer-dominated shocks SNRs (Rakowski 2005; van Adelsberg et al. 2008; Ghavamian et al. 2013) and in situ measurements of Saturn's bow shock

(Masters et al. 2011) reveal the downstream electron-to-ion temperature ratio (hereafter referred to as the temperature ratio) to be in a range of $T_e/T_i \approx 0.05$–0.5, which is well above the Rankine–Hugoniot prediction of $T_e/T_i \approx m_e/m_i$. In our previous studies (Bohdan et al. 2017; Paper II) we reported that the electron temperature observed in PIC simulations is considerably higher than predicted by the Rankine–Hugoniot conditions, but at the same time an energy equipartition between ions and electrons is not reached and electrons are colder than ions. Similar results were demonstrated in the PIC simulations of Kato & Takabe (2010), in which $T_e/T_i \approx 0.33$. These results suggest that superadiabatic electron heating occurs in high-Mach-number shocks.

We have previously discussed that electrons can be accelerated to relativistic energies via a number of mechanisms: SSA (Shimada & Hoshino 2000; Hoshino & Shimada 2002), magnetic reconnection (Matsumoto et al. 2015), stochastic Fermi-like acceleration (SFA; Bohdan et al. 2017), and stochastic shock drift acceleration (Matsumoto et al. 2017). In addition to accelerating particles, these processes cause some amount of electron heating; however, the relative contribution from each is yet to be determined. Electrons also can be heated via the shock potential that is widely discussed in the low-Mach-number regime (Thomsen et al. 1987; Chen et al. 2018; Tran & Sironi 2020).

Electron heating processes are mediated by electromagnetic effects over electron temporal and spatial scales that are much shorter than the ion gyroradius or the ion skin depth. Magnetohydrodynamic (MHD) and hybrid simulations cannot describe physical processes on such small scales. Thus, fully kinetic simulations are needed for a proper description of the electron physics. In this paper we constrain the heating model that aims to predict the temperature ratio at high-Mach-number shocks. The paper is organized as follows. We present a short description of simulation setup in Section 2. The results are presented in Section 3. The discussion and summary are in Section 4.

2. Simulation Setup

Simulations are performed using the modified version of the relativistic electromagnetic TRISTAN code (Buneman 1993) with MPI (Message Passing Interface)-based parallelization (Niemiec et al. 2008; Wieland et al. 2016) and the particle sorting optimization (Dorobisz et al. 2018). The Vay solver (Vay 2008) is used to update particle positions. The triangular-shape-cloud particle shapes (the second-order approximation) and the Friedman (1990) filter for electric and magnetic fields are used to suppress the numerical grid-Cerenkov short-wave radiation. To perform shock simulations we use a 2D3V code configuration that follows two spatial coordinates and all three components of the particle velocities and electromagnetic fields.

The flow–flow simulation setup is used to initialize shocks. Note that the same setup was used in our previous works (Bohdan et al. 2017; Papers I, II, and III), and a more detailed description can be found in Paper I. The simulation setup assumes collision of two counterstreaming electron–ion plasma flows that leads to the formation of two shocks separated by a contact discontinuity. Here we refer to shocks as the *left* and the *right* shocks. The absolute values of the beam velocities are equal, $v_L = v_R = v_0 = 0.2c$. Plasma beams are equal in density, but their temperatures differ by a factor of 1000.

Table 1
Simulation Parameters

Runs	m_i/m_e	M_A	M_s		β_e	
			*1	*2	*1	*2
A1, A2	50	22.6	1104	35	$5 \cdot 10^{-4}$	0.5
B1, B2	100	31.8	1550	49	$5 \cdot 10^{-4}$	0.5
C1, C2	100	46	2242	71	$5 \cdot 10^{-4}$	0.5
D1, D2	200	32	1550	49	$5 \cdot 10^{-4}$	0.5
E1, E2	200	44.9	2191	69	$5 \cdot 10^{-4}$	0.5
F1, F2	400	68.7	3353	106	$5 \cdot 10^{-4}$	0.5

Note. Listed are the ion-to-electron mass ratio m_i/m_e, and Alfvénic, M_A, and sonic Mach numbers, M_s, and the electron plasma beta, β_e. The last two values are shown separately for the left (runs *1) and the right (runs *2) shock. All runs use the in-plane magnetic field configuration, $\varphi = 0°$.

Thus, the *electron* plasma beta (the ratio of the electron plasma pressure to the magnetic pressure) for the left beam is $\beta_{e,L} = 5 \times 10^{-4}$ and $\beta_{e,R} = 0.5$ for the right beam.

The large-scale upstream magnetic field makes an angle $\varphi = 0°$ with the simulation plane (the so-called *in-plane* configuration). Note, that such simulations give us a good representation of the 3D shock physics (Bohdan et al. 2017; Matsumoto et al. 2017). Thus, the adiabatic index is $\Gamma = 5/3$. The resulting shock speed equals $v_{sh} = 0.263c$ in the *upstream* reference frame. The Alfvén velocity is defined as $v_A = B_0/\sqrt{\mu_0(N_e m_e + N_i m_i)}$, where μ_0 is the vacuum permeability, N_i and N_e are the ion and the electron number densities, and B_0 is the far-upstream magnetic field strength. The sound speed reads $c_s = (\Gamma k_B T_i/m_i)^{1/2}$, where k_B is the Boltzmann constant and T_i is the ion temperature defined as $k_B T_i = m_i v_{th}^2/2$, where v_{th} is defined as the most probable speed of the upstream plasma particles in the upstream reference frame. The Alfvénic, $M_A = v_{sh}/v_A$, and sonic, $M_s = v_{sh}/c_s$, Mach numbers of the shocks are defined in the conventional *upstream* reference frame. Note that the *sonic* Mach number, M_s, of the two shocks differs by a factor of $\sqrt{1000} \simeq 30$ because of the difference in β_e.

The ratio of the electron plasma frequency, $\omega_{pe} = \sqrt{e^2 N_e/\epsilon_0 m_e}$, to the electron gyrofrequency, $\Omega_e = eB_0/m_e$, is in the range of $\omega_{pe}/\Omega_e = 8.5$–$17.3$. Here, e is the electron charge, and ϵ_0 is the vacuum permittivity. The electron skin depth in the upstream plasma is constant for all runs and equals $\lambda_{se} = 20\Delta$, where Δ is the size of grid cells. As the unit of length we use the ion skin depth, $\lambda_{si} = \sqrt{m_i/m_e}\,\lambda_{se}$. As the time step $\delta t = 1/40\,\omega_{pe}^{-1}$ is used. The timescales are given in terms of the upstream ion Larmor frequency, $\Omega_i = eB_0/m_i$. The number density in the far-upstream region is 20 particles-per-cell for each species.

In the following sections, we discuss the results of six large-scale numerical experiments (runs A–F), featuring in total 12 physically distinct simulated shocks. We therefore refer to each of these shock cases as a separate simulation run, and label the shocks in the left plasma (cold shock, $\beta_{e,L} = 5 \times 10^{-4}$) with *1, and the right shocks with *2 (warm shock, $\beta_{e,R} = 0.5$). The derived parameters of the simulation runs are listed in Table 1. If a result is valid for both cold and warm shocks we use only a letter without a digit. These simulations cover a wide range of mass ratios ($m_i/m_e = 50$–400) and Alfvénic Mach numbers ($M_A = 22.6$–68.7), thus permitting a thorough investigation of the influence of these parameters on the electron heating processes. The goal of this paper is to clarify these

Table 2
Thermal Properties of the Downstream Plasma

Run	$\frac{k_B T_e}{m_e c^2}$ (Paper II)	$\frac{k_B T_e}{m_e c^2}$ (Equation (13))	T_e/T_i	T_e/T_i (Equation (16))
A1	0.107 ± 0.004	0.1 ± 0.03	0.17 ± 0.04	0.16 ± 0.05
A2	0.091 ± 0.004		0.14 ± 0.03	
B1	0.216 ± 0.004	0.19 ± 0.05	0.18 ± 0.03	0.16 ± 0.05
B2	0.183 ± 0.004		0.15 ± 0.03	
C1	0.253 ± 0.002	0.22 ± 0.07	0.19 ± 0.03	0.19 ± 0.06
C2	0.217 ± 0.003		0.17 ± 0.02	
D1	0.332 ± 0.024	0.34 ± 0.08	0.15 ± 0.03	0.15 ± 0.04
D2	0.28 ± 0.003		0.11 ± 0.01	
E1	0.394 ± 0.005	0.38 ± 0.1	0.16 ± 0.02	0.17 ± 0.05
E2	0.368 ± 0.009		0.16 ± 0.02	
F1	0.765 ± 0.035	0.8 ± 0.2	0.18 ± 0.04	0.18 ± 0.06
F2	0.732 ± 0.02		0.18 ± 0.04	

Note. Second column—the downstream electron temperatures listed in Paper II. Third column—the downstream electron temperature calculated via Equation (13). Fourth column—the electron-to-ion temperature ratio observed in simulations. Fifth column—the electron-to-ion temperature ratio calculated via Equation (16).

dependencies in order to give a prediction for realistic high-Mach-number shocks.

3. Results

In Paper II we showed that the downstream electron temperature is approximately proportional to the mass ratio; therefore, a similar fraction of the upstream ion kinetic energy is transferred to thermal electrons in the simulations discussed here. It also results in similar temperature ratios in all runs (see Table 2).

Here we want to constrain the electron heating model based on simulation data. First, we identify the processes responsible for the electron heating. Next, using known properties of mechanisms and particle data, we determine how individual heating efficiencies depend on the mass ratio (m_i/m_e), Alfvénic Mach number (M_A), and the shock velocity (v_{sh}). Finally, using energy gains from individual heating processes, we calculate numerical coefficients for them in order to confirm the heating model and simulation results.

Using these principles we express the energy gain provided by the individual processes in the form of

$$\varepsilon_a = \alpha_a F_a m_i v_{sh}^2, \tag{1}$$

where index a denotes the heating process, α_a is a numerical coefficient, and $F_a \equiv F_a(M_A, m_i/m_e, v_{sh})$ stands for the scaling properties of the heating process. Note that energy increments strongly vary during the shock self-reformation cycle, and in our calculation we use values averaged over one reformation period. Error bars for the numerical coefficients α_a reflect the dispersion of simulation results projected on the heating model.

3.1. Electron Energy Evolution

We use the energy history of electrons selected in the shock upstream of run B2 (Figure 1) for demonstration of the main stages of the electron heating. Electrons reside at the leading edge of the shock foot with electrostatic Buneman waves at t_1 (panel (a1)), the Weibel instability region of the foot at t_2 (panel (a2)), the ramp region where magnetic reconnection occurs at t_3 (panel (a3)), the turbulent postovershoot at t_4 (panel (a4)), and the downstream at t_5 (panel (a5)).

Particle energies change due to work, W_{tot}, done by the electric field. For identification of heating process we split this work into two parts, namely, the work done in the directions parallel, $W_\parallel$, and perpendicular, $W_\perp$, to the local magnetic field. Therefore, the electron kinetic energy is calculated as

$$\varepsilon = W_{tot} + \varepsilon_0 = W_\parallel + W_\perp + \varepsilon_0, \tag{2}$$

where ε_0 is an initial kinetic energy, $W_\parallel = \int_{t'=0}^{t} eE_\parallel v_\parallel dt'$, and $W_\perp = \int_{t'=0}^{t} eE_\perp v_\perp dt'$. All variables denoted with $\perp$or $\parallel$ are vector components perpendicular and parallel to the local magnetic field, respectively.

The total energy change of the electron population is represented by W_{tot} in Figure 1(b). The energy of the electrons starts to grow when they enter the shock foot at t_2 (panel (a2)). Figure 1(b) shows that the energy reaches the maximal value at $\Omega_i t \approx 3.7$ when particles reside in the shock overshoot, and then it gradually decreases when electrons are advected to the shock downstream. At the final step about 70% of the total energy is produced by parallel heating and the remaining part has a perpendicular origin.

We have identified five processes responsible for the electron heating: SSA via interaction with Buneman waves at the leading edge of the shock foot, a heating by the shock potential at the shock foot and the ramp, magnetic reconnection in the shock ramp, SFA in the shock ramp and the overshoot, and an adiabatic heating that follows plasma compression and decompression.

Note, that Figure 1 is a representative example of energy behavior for the selected electron population. The evolution of the energy components presented in panels (b)–(d) strongly depends on the phase of shock self-reformation. Therefore, we always consider averaged values.

3.2. Heating via SSA

The Buneman instability is excited because of the relative motion of the upstream electrons to the reflected ions. The energy budget available from this process approximately given by $E_{SSA,avail} \approx 2m_e v_{sh}^2 \simeq 0.15 m_e c^2$ (Amano & Hoshino 2009). Later this energy is converted into electron heating; therefore, it can be used as an upper limit for the energy provided to electrons via SSA. In Paper II we discussed that only about 1% of the available energy is transferred to the *nonthermal* high-energy electrons. However, in this case we are interested in the *total* energy gain, which is about $0.1E_{SSA,avail}$ for the selected population of electrons. Thus, we estimate the energy gain via SSA as

$$\varepsilon_{SSA} \approx \alpha_{SSA} m_e v_{sh}^2 = \alpha_{SSA} \frac{m_e}{m_i} m_i v_{sh}^2, \tag{3}$$

where α_{SSA} depends on the magnetic field configuration of the simulation and it equals $\alpha_{SSA,0} = 0.2 \pm 0.1$ for the in-plane case, where the subscript "0" denotes the angle of the initial magnetic field to the simulation plane. For the selected electron set the heating via SSA takes place at $\Omega_i t \approx 3$; it is not well visible in Figure 1 because of the very small efficiency

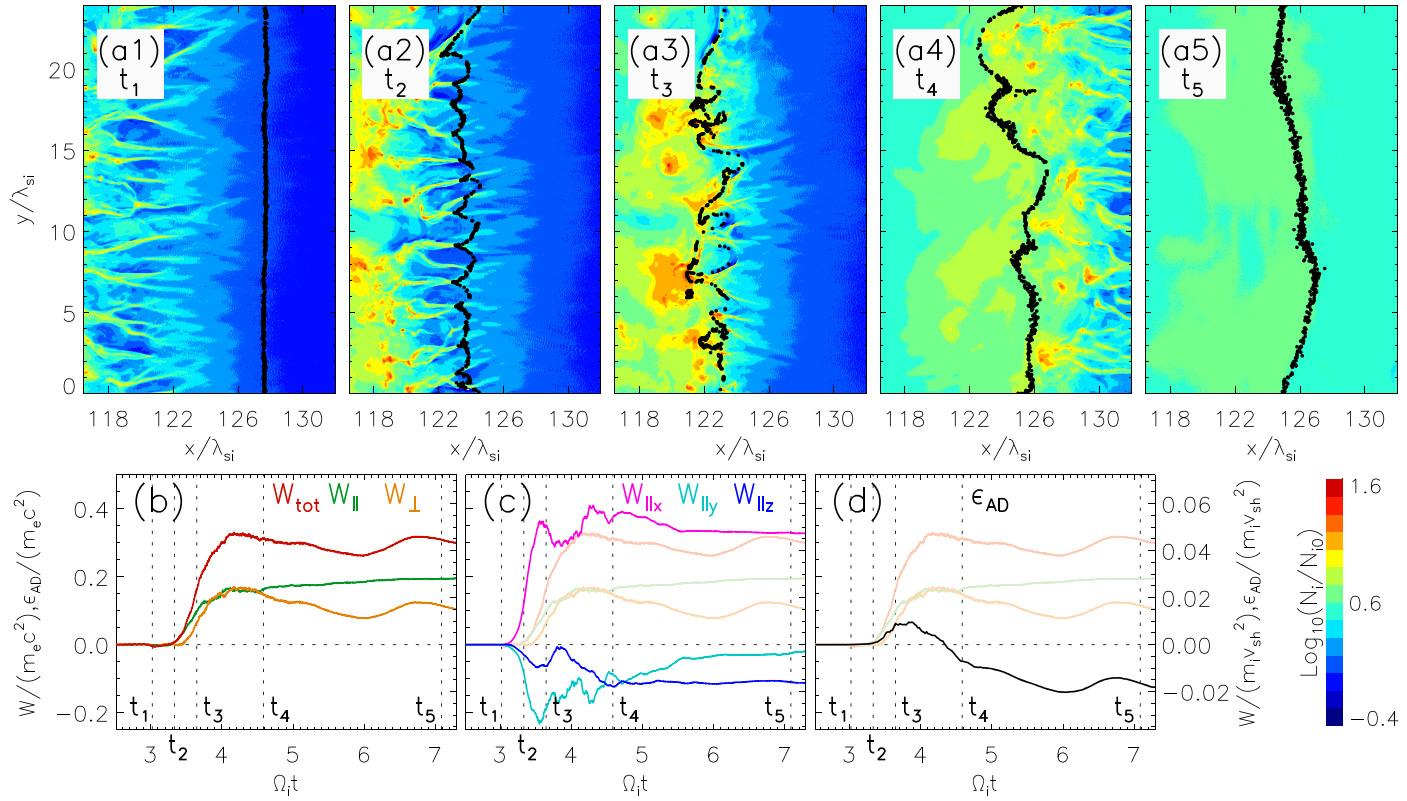

Figure 1. Evolution of the work components of traced electrons for run B2. Panels (a1)–(a5) present the positions of traced electrons (black dots) at the time t_1–t_5 on density maps of the shock region. Panel (b): the temporal evolution of the total work done by electric field ($W_{\rm tot}$, red line), the parallel work component ($W_{\parallel}$, green line), and the perpendicular work component ($W_{\perp}$, orange line). Panel (c): magenta, light blue, and dark blue lines are x- ($W_{\parallel x}$), y- ($W_{\parallel y}$), and z-components ($W_{\parallel z}$) of the parallel work. Panel (d): evolution of the adiabatic component (W_{AD}; see Section 3.6). Faded curves in panels (c) and (d) represent lines from panel (b). Scales for the bottom panels are given in terms of $m_{\rm e}c^2$ and $m_{\rm i}v_{\rm sh}^2$. The vertical dashed lines in panels (b), (c), and (d) are time markers for $t_1 - t_5$; the horizontal dashed line is the zero level.

compared to other processes. Note that SSA contributes to the perpendicular work component. It is also easy to see from Equation (3) that the heating due to SSA may contribute a substantial amount of energy only in case of small mass ratios.

Previously we demonstrated in Bohdan et al. (2017) and Matsumoto et al. (2017) that the realistic 3D SSA efficiency is reproduced in simulations with an out-of-plane magnetic field configuration ($\varphi = 90^\circ$) where Buneman waves are well captured in the simulation plane. In runs with such a field configuration, the heating efficiency is higher, with around 50% of the available energy transferred and $\alpha_{\rm SSA,90} = 1 \pm 0.5$. This value we put in the heating model of realistic shocks.

3.3. Heating by the Shock Potential

In our simulations electrons are magnetized, thus they follow the initial magnetic flux tube and can freely move only along magnetic field lines. Therefore, if any plasma disturbance creates regions with aligned magnetic and electric fields (which initially are perpendicular to each other) electrons can be energized via parallel heating. At a shock transition of high-Mach-number shocks the Weibel instability and magnetic reconnection are responsible for generation of turbulent magnetic fields

In Figure 1(a2), the electron positions show that magnetic field lines are deformed because of additional B_x and B_z components generated by the Weibel instability. Furthermore, the shock potential (E_x) starts to operate in this region. The magnetic field structure is represented by nonpropagating

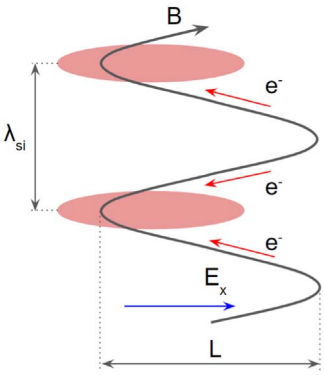

Figure 2. Scheme of electron heating by the shock potential in the shock foot. Red ellipses indicate dense Weibel filaments. The motions of electrons are designated by red arrows. The blue arrow is the shock potential, E_x, in the shock foot. $\lambda_{\rm si}$ represents the Weibel instability wavelength and L is a measure of a magnetic field line widening because of B_x amplification.

linearly polarized magnetic field waves generated by the Weibel instability (Figure 2). This field is regular with the spatial scale of $\lambda_{\rm si}$. Deeper in the shock, compressions and magnetic reconnection make the magnetic field structure more turbulent and chaotic (Figure 1(a3)). Therefore, the initial upstream field configuration is destroyed in the shock transition, creating suitable conditions for the parallel heating of electrons.

Parallel acceleration for the selected portion of electrons occurs in two stages. During the first stage, $\Omega_{\rm i}t = 3.1$–3.6,

electrons reside in the shock foot with the regular filamentary magnetic field produced by the Weibel instability. The electron energy increases because of a rapid growth of $W_{\parallel}$. During the second stage, $\Omega_i t = 3.6$–5, electrons are at the shock ramp-overshoot, where the magnetic field is turbulent, and $W_{\parallel}$ grows slower than in the first stage. Here we call these parts of the parallel work as the regular component, $\varepsilon_{\rm SP,r}$, and the turbulent component, $\varepsilon_{\rm SP,t}$, because of the magnetic field structure at the corresponding regions. Note that "SP" refers to the shock potential.

While the Weibel instability develops, electrons are moving to the left and forming dense filaments (Figure 2). During this motion they gain some energy because of the work done by the E_x-field (see $W_{\parallel,x}$ in Figure 1(c)). We found that in this region $W_{\parallel,x}$ is always the main energy contributor and for further discussions we ignore $W_{\parallel,y}$ and $W_{\parallel,z}$. Thus, the energy income is

$$\varepsilon_{\rm SP,r} \propto eE_x L = eE_x \frac{B_x}{B_y}\frac{\lambda_{\rm si}}{2} \propto eE_x M_{\rm A}\frac{\lambda_{\rm si}}{2} \propto \frac{1}{2} m_{\rm i} v_{\rm sh}^2. \quad (4)$$

Here we use two relations derived from simulation data. The saturation level of the normalized B_x generated by the Weibel instability is roughly proportional to the Alfvénic Mach number, so the ratio of $\frac{1}{M_{\rm A}}\frac{B_x}{B_y}$ is constant. We also can express E_x in terms of the upstream fields. The shock potential, $e\phi$, is proportional to the ion upstream kinetic energy. We can therefore estimate the electric field as $E_x \propto \phi/L_{\rm ramp} \propto r_{\rm g} = v_{\rm sh}/\Omega_{\rm i}$, then $E_x = \eta v_{\rm sh} B_0$. In Paper III we discussed that all shocks host very similar conditions at the shock ramp, namely, the same fraction of reflected ions, the same relative velocities, etc. Therefore, the coefficient η appears to be the same in our simulations.

Using the observed parallel energy income during this stage, we can derive the regular heating component:

$$\varepsilon_{\rm SP,r} = \alpha_{\rm SP,r} m_{\rm i} v_{\rm sh}^2, \quad (5)$$

where $\alpha_{\rm SP,r} = 0.012 \pm 0.002$.

The ramp-overshoot region is strongly turbulent; thus, the scheme presented in Figure 2 is no longer valid. However, the thorough investigation of $W_{\parallel}$ in this region demonstrates that the main energy contributor is still the x-component of the electric field. Note that part of $W_{\parallel}$ during the second stage originates from magnetic reconnection (see Section 3.4), but we account for it in our calculations.

As soon as the magnetic field is turbulent electrons have a possibility to move some distance along the x-axis, which is proportional to the length of the turbulent region, $L \approx L_{\rm ramp} \propto r_{\rm gi} = M_{\rm A}\lambda_{\rm si}$. As we discussed above the average electric field is proportional to the upstream electric field, $E'_x \propto v_{\rm sh} B_0$. The only difference is that this field is opposite (negative) to the shock potential that heats electrons during the first stage. Therefore, the chaotic component is also proportional to the upstream ion kinetic energy, $\varepsilon_{\rm SP,t} \propto m_{\rm i} v_{\rm sh}^2$. Using the simulation data we can write that

$$\varepsilon_{\rm SP,t} = \alpha_{\rm SP,t} m_{\rm i} v_{\rm sh}^2, \quad (6)$$

where $\alpha_{\rm SP,t} = 0.013 \pm 0.002$, which is consistent (as error bars overlap) with what we estimated for the regular component. Such a result is not surprising because during this process the magnetic field lines are straightening and the electrons are redistributed back evenly along the magnetic field lines in the presence of a negatively directed E_x. It is essentially the opposite to what happens in the Weibel instability region, albeit in more turbulent and chaotic way.

3.4. Heating by Magnetic Reconnection

In Paper III we discussed how magnetic reconnection accelerates electrons to nonthermal energies. We also found that magnetic reconnection becomes more active in shocks with high Alfvénic Mach numbers and the fraction of electrons involved in magnetic reconnection correlates with $M_{\rm A}$. It makes the heating via magnetic reconnection strongly dependent on Alfvénic Mach number.

For the selected electron population, magnetic reconnection takes place at $\Omega_i t \approx 3.5$–3.6. In Paper III we discussed that magnetic reconnection can contribute both to $W_{\perp}$ (e.g., Fermi-like processes) and $W_{\parallel}$ (e.g., parallel heating at x-points). For run B2 the average energy of the electrons that have undergone reconnection is $0.21 m_{\rm e} c^2$. Heating via SSA and the regular part of the shock potential occurs before magnetic reconnection; thus, the energy gained by electrons due to magnetic reconnection is $\varepsilon_{\rm MR,sim} = 0.21 m_{\rm e} c^2 - \varepsilon_{\rm SSA} - \varepsilon_{\rm SP,r} = 0.115 m_{\rm e} c^2$. Taking into account that about 26% (see Paper III) of electrons are involved in magnetic reconnection, the fraction of the total heating delivered by magnetic reconnection is about 11% in run B2.

The number of vortices generated during magnetic reconnection differs by a factor of 60 between runs A and F (see Table 2 in Paper III). However, the heating efficiency grows not so quickly. Magnetic reconnection gives 6% of the total heating in runs A, 11% in runs B, 18% in runs C, 15% in runs D, 17% in runs E, and 20% in runs F. This happens because the electron temperature at reconnection sites, $T_{\rm MR}$, becomes smaller compared to the downstream electron temperature, T_e, in high $M_{\rm A}$ cases. $T_{\rm MR}/T_e$ is about 1 in runs A and 0.5 in runs F.

To approximate the heating via magnetic reconnection we also need to determine boundary conditions. We assume that magnetic reconnection is switched off when $M_{\rm A} < 20$; in Paper III we have already demonstrated that in run A the number of reconnection sites is very small and it drops quickly. In the high-Mach-number limit ($M_{\rm A} \gtrsim 100$), we expect saturation of magnetic reconnection efficiency at a level that does not exceed 25%, because already in run F almost all electrons are involved in the process and the ratio $T_{\rm MR}/T_e$ will likely stabilize around 0.5. Therefore, the heating due to magnetic reconnection we estimate as

$$\varepsilon_{\rm MR} = \alpha_{\rm MR} m_{\rm i} v_{\rm sh}^2,$$
$$\alpha_{\rm MR} = \begin{cases} 0, & M_{\rm A} < 20 \\ \alpha^*_{\rm MR}(M_{\rm A} - 20)^{\frac{1}{3}}, & 20 < M_{\rm A} < 100, \\ \alpha^*_{\rm MR} 80^{\frac{1}{3}}, & M_{\rm A} > 100 \end{cases} \quad (7)$$

where $\alpha^*_{\rm MR} = (22 \pm 4) \cdot 10^{-4}$. For the discussion of the heating model in Section 3.7 we assume that magnetic reconnection contributes equally to $W_{\perp}$ and $W_{\parallel}$.

3.5. Heating via SFA

In Bohdan et al. (2017) we have discussed that high-energy electrons are accelerated via SFA. However, this process works regardless of the particle energy and also contributes to the electron heating.

During the time interval of $\Omega_i t \approx 3.6$–4.5 the electrons are in the shock ramp-overshoot region (Figures 1(a3) and (a4)) and the perpendicular work component grows (Figure 1(b)). This region is characterized by a turbulent magnetic field hosting appropriate conditions for SFA. When a particle interacts with moving magnetic field structures it is accelerated by a motional electric field, $\boldsymbol{E} = -\boldsymbol{v} \times \boldsymbol{B}$; thus, SFA contributes to $W_\perp$.

To estimate the energy income in SFA we need to know the number of collisions of electron with scattering centers, $N_{\rm coll}$, and the average velocity of these centers, $v_{\rm mag}$. The energy income via SFA is

$$\frac{\varepsilon_{\rm SFA}}{\varepsilon_e} \propto \left(\frac{v_{\rm mag}}{v_e}\right)^2 N_{\rm coll} = \left(\frac{v_{\rm mag}}{v_e}\right)^2 \frac{T}{\Delta t} \propto \left(\frac{v_{\rm mag}}{v_e}\right)^2 \frac{r_{\rm gi} v_e}{v_{\rm sh} \lambda_{\rm si}} = M_{\rm A} \frac{v_{\rm mag}^2}{v_e v_{\rm sh}}, \quad (8)$$

where ε_e and v_e are the electron energy and velocity before SFA; $N_{\rm coll} = T/\Delta t$, where $T \propto r_{\rm gi}/v_{\rm sh}$ is the total time an electron spends in the shock transition; $\Delta t \propto \lambda_{\rm si}/v_e$ is the average time between collisions, where the average distance between scattering centers are defined by Weibel instability with the spatial scale of $\lambda_{\rm si}$. In our simulations we found that $v_{\rm mag}$ does not depend on the mass ratio or Mach number and it can be represented as $v_{\rm mag} = \chi v_{\rm sh}$, where $\chi \approx 0.25$ was derived from simulations.

Heating by SFA occurs after energization by SSA, the regular part of the shock potential, and magnetic reconnection; thus, we can assume that the initial energy for SFA is $\varepsilon_e = (m_{\rm e} v_e^2)/2 = \varepsilon_{\rm SSA} + \varepsilon_{\rm SP,r} + \varepsilon_{\rm MR}$. Therefore, the energy income from SFA is

$$\varepsilon_{\rm SFA} = \alpha_{\rm SFA} m_{\rm i} v_{\rm sh}^2, \quad \alpha_{\rm SFA} = \alpha^*_{\rm SFA} M_{\rm A} \chi^2 \sqrt{\frac{(\alpha_{\rm SSA} + \alpha_{\rm SP,r} + \alpha_{\rm MR}) m_{\rm e}}{2 m_{\rm i}}} \quad (9)$$

where $\alpha^*_{\rm SFA} = 0.7 \pm 0.2$.

Here we used nonrelativistic formulas because relativistic corrections cause only minor adjustments for the cases discussed here, and SNR or planetary bow shocks are nonrelativistic.

3.6. Adiabatic Heating

In the shock transition plasma is compressed; thus, we need to account for heating because of adiabatic compression. During compression the plasma temperature can be approximated by

$$TV^{\Gamma-1} = \text{const}, \quad (10)$$

where V is the volume of the flux tube and $\Gamma = 5/3$ is the adiabatic index. Using the total derivative of Equation (10) we estimate the energy income from adiabatic compression as

$$\varepsilon_{\rm AD} = \sum_n \varepsilon_{{\rm AD},n}, \quad \varepsilon_{{\rm AD},n} = k_{\rm B} T_n \left(1 - \frac{V_{n+1}}{V_n}\right). \quad (11)$$

and the sum is calculated over time steps corresponding to the electrons traveling from the upstream to the downstream. Here we use B-field maps to derive the volume of the flux tube and the traced particle data to estimate the electron temperature inside the selected flux tube.

The overall impact of a compression–decompression cycle appears to be negative (Figure 1(d)). Such a result is slightly counterintuitive; however, it can happen if an additional heating process operates during a compression–decompression cycle. Initially the electron temperature is low; thus, the adiabatic heating during compression is also low. However, decompression happens when electrons cross the shock overshoot and they are already hot. Therefore, the adiabatic cooling is high and in our case it overcomes the adiabatic heating during the compression. It results in an overall negative impact of the compression–decompression cycle.

As expected, the behavior of the adiabatic energy income is consistent with $W_\perp$ and $W_{\rm tot}$ in the shock downstream ($\Omega_i t > 5$) where only adiabatic compression and decompression are responsible for the electron energy change.

Compression operates on top of all prior discussed processes, and the adiabatic influence can be represented as a modulation of energy incomes from processes contributing to $W_\perp$. Thus,

$$W_\perp = \alpha_{\rm AD} \varepsilon_\perp, \quad \alpha_{\rm AD} = 0.6 \pm 0.1, \quad (12)$$

where $\varepsilon_\perp$ is the sum of energy incomes from processes contributing to $W_\perp$.

3.7. Model of the Electron Heating

To compile the heating model we combine all individual heating efficiencies (Equations (3), (5), (6), (7), (9), and (12)). Recall that both shock potential components contribute to the parallel work, magnetic reconnection contributes equally to the parallel and perpendicular parts, and SSA, SFA, and adiabatic heating affect on the perpendicular component. Therefore, combining Equations (2) and (12) with the consideration described above we can derive

$$W_{\rm tot} = \varepsilon_{\rm SP,r} + \varepsilon_{\rm SP,t} + \varepsilon_{\rm MR}/2 + \alpha_{\rm AD}(\varepsilon_{\rm SSA} + \varepsilon_{\rm SFA} + \varepsilon_{\rm MR}/2), \quad (13)$$

and the downstream electron temperature reads

$$k_{\rm B} T_e = \frac{2}{3}(W_{\rm tot} + \varepsilon_0). \quad (14)$$

The amount of available energy for the particle heating is defined by Rankine–Hugoniot relations, namely, by the ion temperature jump condition. The available energy is

$$E_{\rm avail} = \frac{3}{2} T_i = \frac{3}{2} \cdot \frac{5}{16} M_{\rm s}^2 T_{{\rm up},i} = \frac{1}{2} m_{\rm i} v_0^2. \quad (15)$$

Thus, in the downstream reference frame, where our simulations are performed, the upstream ion kinetic energy is the

source for the downstream thermal energies of ions and electrons. Therefore, the temperature ratio can be calculated as

$$\frac{T_e}{T_i} = \frac{W_{tot}}{E_{avail} - W_{tot}}. \quad (16)$$

To derive Equations (15) and (16) we neglected the upstream electron kinetic energy, the upstream ion thermal energy in the shock upstream, energies of electric and magnetic fields that are small compared to other components.

The modeled downstream temperatures and temperature ratios are listed in Table 2, and predictions of the heating model are consistent with the simulation results.

4. Summary and Discussion

This work is the fourth paper in a series investigating the physics of nonrelativistic perpendicular high-Mach-number shocks. In our previous studies, we discussed the production of nonthermal electrons via SSA operating at the shock foot (Papers I and II) and via magnetic reconnection resulting from the nonlinear decay of ion Weibel filaments at the shock ramp (Paper III). In this paper, we investigate superadiabatic electron heating. We constrain the heating model for the downstream electron-to-ion temperature ratio in realistic high-Mach-number shocks. 2D simulations with an in-plane magnetic field configuration are capable of reproducing the main shock structures found in 3D simulations (Bohdan et al. 2017; Matsumoto et al. 2017), and therefore electron heating is also well captured at a fraction of the computational expense. Our simulations are performed for a wide range of physical parameters ($m_i/m_e = 50$–400 and $M_A = 22.6$–68.7). which permits predictions for realistic shocks.

In Paper II we discussed that all shocks demonstrate superadiabatic electron heating, and that the downstream electron temperature is well above that predicted by the Rankine–Hugoniot condition. Here we calculate the downstream temperature ratio that is in range of $T_e/T_i = 0.11$–0.19.

Electrons are heated via SSA, parallel acceleration due to the shock potential, magnetic reconnection, and SFA. Electrons energized via SSA, magnetic reconnection, and SFA have been already extensively studied, and here heating via the shock potential at the shock foot is discussed for the first time. At perpendicular shocks the upstream magnetic field and the shock potential are perpendicular to each other. Nevertheless, operating at the shock foot, the Weibel instability generates a B_x magnetic field component that permits parallel heating by the shock potential. It consists of a regular part that deals with ordered Weibel filaments at the shock foot and a turbulent part that operates deeper in the turbulent ramp-overshoot region.

In addition to these processes, compression at the shock transition influences the plasma temperature, but its total effect is surprisingly negative. During passage from the upstream to the downstream regions, plasma is compressed to the overshoot density ($N_{max}/N_0 \approx 8$) and then relaxes and reaches a compression ratio of 4 expected for high Mach numbers. The adiabatic heating at the compression stage is smaller than cooling after the shock overshoot, on account of nonadiabatic heating in between, hence the net adiabatic cooling.

Among these processes only SSA is limited by the *electron* upstream kinetic energy as the instability is driven by inbound electrons. All other processes are the ion-related phenomena, and the incoming energy is proportional to the *ion* upstream kinetic energy. They are actually responsible for the superadiabatic electron heating. Combining all detected heating processes we constrain the heating model. It accurately predicts the downstream electron temperature of perpendicular nonrelativistic high-Mach-number shocks performed by means of PIC simulations.

We apply the heating model to realistic shocks using the real proton-to-electron mass ratio and assuming that heating processes are not significantly different between our 2D in-plane shock simulations and real 3D shocks. In SNR shocks with a propagation velocity above 1000 km s^{-1}, which are more than likely to be high-Mach-number shocks, the observed temperature ratio is $T_e/T_i = 0.05$–0.2 (Rakowski 2005; van Adelsberg et al. 2008; Ghavamian et al. 2013), based on X-ray spectra for T_e and Balmer-line width for T_i. We do not precisely know the Alfvénic Mach number of SNR shocks, and so we simply assume that it is above 20. The predicted temperature ratio is $T_e/T_i = 0.09$–0.25 for $M_A > 20$, which indicates a good match between observations and PIC simulations.

At Alfvénic Mach numbers $M_A > 100$ the Weibel instability is heavily saturated, which limits parallel heating by the shock potential and magnetic reconnection, and the slow growth of the electron/ion temperature ratio in our model would not necessarily continue. For $20 < M_A < 100$ our model predicts that the temperature ratio is independent of the shock velocity. We do not reproduce empirically (van Adelsberg et al. 2008) and theoretically (Vink et al. 2015) the predicted relation of $T_e/T_i \propto v_{sh}^{-2}$, which for the standard jump conditions for T_i is equivalent to stating that T_e is independent of v_{sh}, and hence electron heating is not governed by the bulk kinetic energy supply of inbound particles. Instead, we see that the electron temperature is roughly proportional to the ion upstream kinetic energy. Caution is advised when comparing the temperature ratio immediately downstream of the shock, which is measured in our simulations, with that found in observations that reflects the state of plasma a few months or years after passage through the shock. Note also that the calculations by Vink et al. (2015) rely on shock thermodynamics only and ignore the shock heating mechanisms themselves.

The solar system also hosts high-Mach-number shocks. One of the best-studied examples is Saturn's bow shock whose properties have been measured in situ by the Cassini spacecraft. The plasma beta upstream of Saturn's bow shock is about 0.1 (Jackman & Arridge 2011), which is within the parameter range of our simulations. The postshock temperature ratio for the quasi-perpendicular Saturn's bow shock was published by Masters et al. (2011). Figure 3 shows a comparison of the heating model with these data. For comparison, we consider cases when the shock has a high Mach number ($M_A > 20$) and is quasi-perpendicular ($\theta_{B_n} > 45°$), which severely limits the number of data points. Cassini can only measure the electron temperature. The ion temperature is inferred from the shock speed that itself is an estimate requiring transformation from the spacecraft frame to the shock frame. To indicate the level of correction that Masters et al. (2011) had to impose, we add to Figure 3 gray arrows that undo those changes and point to the original measurement. Some data points are consistent within the error bars provided by our model, but two values are below the prediction. This may happen for a few reasons. First, our simulations consider only perpendicular shocks, but the inferred shock obliquity for the shock crossings shown in Figure 3 is in the range $55° < \theta_{B_n} < 80°$. Secondly, in our

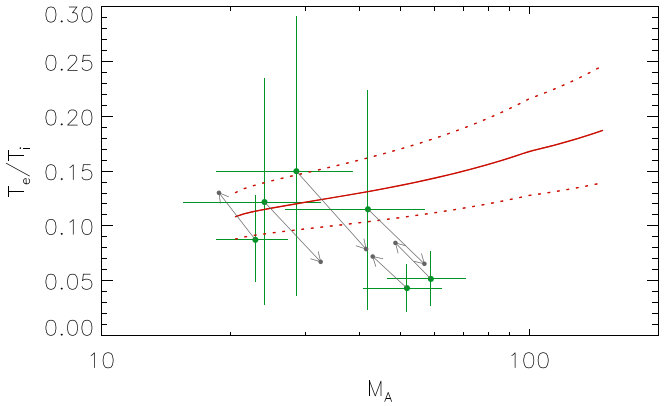

Figure 3. Comparison of the model temperature ratio with Cassini measurements during Saturn's bow shock crossings with $M_A > 20$ and $\theta_{B_n} > 45°$ (Masters et al. 2011). Red solid line represents the heating model (Equation (16)), and red dotted lines are the error bars. Green dots are Cassini measurements, with black arrows pointing to the uncorrected values.

simulations shocks propagate into homogeneous media, and we cannot account for density or field fluctuations, both of which are present upstream of real shocks, that may have an impact on the temperature ratio. These assumptions therefore lead to additional uncertainties in our calculations of the temperature ratio. Nevertheless, we can state here that the heating model yields a reasonably good estimate of the temperature ratio at quasi-perpendicular high-Mach-number shocks.

The authors thank Adam Masters and Ali Sulaiman for providing Saturn bow shock data. Great thanks to Aaron Tran, Lorenzo Sironi, Anatoly Spitkovsky, and Vassilis Tsiolis for fruitful discussions. The work of J.N. has been supported by Narodowe Centrum Nauki through research project 2019/33/B/ST9/02569. This work was supported by JSPS-PAN Bilateral Joint Research Project grant No. 180500000671. This research was supported by PLGrid Infrastructure. The numerical experiment was possible through a 10 Mcore-hour allocation on the 2.399 PFlop Prometheus system at ACC Cyfronet AGH. Part of the numerical work was conducted on resources provided by the North-German Supercomputing Alliance (HLRN) under projects bbp00014 and bbp00033.

ORCID iDs

Artem Bohdan https://orcid.org/0000-0002-5680-0766
Martin Pohl https://orcid.org/0000-0001-7861-1707
Jacek Niemiec https://orcid.org/0000-0001-6036-8569
Paul J. Morris https://orcid.org/0000-0002-8533-8232
Yosuke Matsumoto https://orcid.org/0000-0002-1484-7056
Takanobu Amano https://orcid.org/0000-0002-2140-6961
Masahiro Hoshino https://orcid.org/0000-0002-1818-9927

References

Amano, T., & Hoshino, M. 2009, ApJ, 690, 244
Bohdan, A., Niemiec, J., Kobzar, O., & Pohl, M. 2017, ApJ, 847, 71
Bohdan, A., Niemiec, J., Pohl, M., et al. 2019a, ApJ, 878, 5
Bohdan, A., Niemiec, J., Pohl, M., et al. 2019b, ApJ, 885, 10
Bohdan, A., Pohl, M., Niemiec, J., et al. 2020, ApJ, 893, 6
Buneman, O. 1958, PhRvL, 1, 8
Buneman, O. 1993, in Computer Space Plasma Physics: Simulation Techniques and Software, Vol. 67, ed. H. Matsumoto & Y. Omura (Tokyo: Terra Scientific)
Chen, L. J., Wang, S., Wilson, L. B., et al. 2018, PhRvL, 120, 225101
Dorobisz, A., Kotwica, M., Niemiec, J., et al. 2018, in Parallel Processing and Applied Mathematics, ed. R. Wyrzykowski et al. (Berlin: Springer),
Fried, B. D. 1959, PhFl, 2, 337
Friedman, A. 1990, in US-Japan Workshop on Advanced Computer Simulation Techniques Applied to Plasmas and Fusion (Vienna: IAEA)
Ghavamian, P., Schwartz, S. J., Mitchell, J., Masters, A., & Laming, J. M. 2013, SSRv, 178, 633
Hoshino, M., & Shimada, N. 2002, ApJ, 572, 880
Jackman, C. M., & Arridge, C. S. 2011, SoPh, 274, 481
Kato, T. N., & Takabe, H. 2010, ApJ, 721, 828
Marshall, W. 1955, RSPSA, 233, 367
Masters, A., Schwartz, S. J., Henley, E. M., et al. 2011, JGRA, 116, A10107
Matsumoto, Y., Amano, T., Kato, T. N., & Hoshino, M. 2015, Sci, 347, 974
Matsumoto, Y., Amano, T., Kato, T. N., & Hoshino, M. 2017, PhRvL, 119, 105101
Niemiec, J., Pohl, M., Stroman, T., & Nishikawa, K.-I. 2008, ApJ, 684, 1174
Rakowski, C. E. 2005, AdSpR, 35, 1017
Schwartz, S. J., Thomsen, M. F., Bame, S. J., & Stansberry, J. 1988, JGR, 93, 12923
Shimada, N., & Hoshino, M. 2000, ApJL, 543, L67
Thomsen, M. F., Mellott, M. M., Stansberry, J. A., et al. 1987, JGR, 92, 10119
Tran, A., & Sironi, L. 2020, ApJL, 900, L36
van Adelsberg, M., Heng, K., McCray, R., & Raymond, J. C. 2008, ApJ, 689, 1089
Vay, J. L. 2008, PhPl, 15, 056701
Vink, J., Broersen, S., Bykov, A., & Gabici, S. 2015, A&A, 579, A13
Wieland, V., Pohl, M., Niemiec, J., Rafighi, I., & Nishikawa, K.-I. 2016, ApJ, 820, 62